Low-voltage, broadband graphene-coated Bragg mirror electro-optic modulator at telecom wavelengths

Thomas Wood, Jérémy Lhuillier, Malik Kemiche, Pierre Demongodin, Bertrand Vilquin, Pédro Rojo Romeo, Ali Belarouci, Lotfi Berguiga, Ségolène Callard, Xavier Letartre, et al.

HAL Id: hal-02961285
https://hal.science/hal-02961285

Submitted on 8 Oct 2020

Low-voltage, broadband graphene-coated Bragg mirror electro-optic modulator at telecom wavelengths

Thomas Wood,[1,*] Jérémy Lhuillier,[1] Malik Kemiche,[1] Pierre Demongodin,[1] Bertrand Vilquin,[1] Pedro Rojo Romeo,[1] Ali Belarouci,[1] Lotfi Berguiga,[2] Ségolène Callard,[1] Xavier Letartre,[1] and Christelle Monat[1]

[1]*Institut des Nanotechnologies de Lyon, CNRS UMR5270, École Centrale Lyon, 69134 Écully, France*
[2]*Institut des Nanotechnologies de Lyon, CNRS UMR5270, INSA de Lyon, 69621 Villeurbanne, France*
[*]*tomwood321@hotmail.com*

Abstract: We demonstrate a graphene based electro-optic free-space modulator yielding a reflectance contrast of 20% over a strikingly large 250nm wavelength range, centered in the near-infrared telecom band. Our device is based on the original association of a planar Bragg reflector, topped with an electrically contacted double-layer graphene capacitor structure employing a high work-function oxide shown to confer a static doping to the graphene in the absence of an external bias, thereby reducing the switching voltage range to +/-1V. The device design, fabrication and opto-electric characterization is presented, and its behavior modeled using a coupled optical-electronic framework.

1. Introduction

Since the isolation of graphene monolayers in 2004, attention has turned to embedding this 2D material into optical telecommunications components such as modulators, frequency convertors and optical clocks [1,2]. Indeed, graphene exhibits some remarkable optical properties such as wideband optical absorption in both normal-incidence (ideal for free-space applications [3]) and grazing-incidence (suited to waveguide based applications [4]), intrinsic supporting of surface plasmon polariton waves [5,6], and a full catalogue of non-linear optical properties [7] including saturable absorption and photon mixing phenomena. These optical properties can be activated and deactivated for a given free space wavelength by "doping" graphene using the same gating techniques developed for solid state electronics; for example, in the case of absorption modulation, one must shift the Fermi level such that its separation from the Dirac point in energy (called the chemical potential, μ) is equal to at least half the photon energy in order to render graphene transparent [2,8]. Nonetheless, as an atomically thin monolayer, graphene's limited interaction with light in free space restricts its absorption to 2.3% across a wide spectral range for un-doped samples [9].

A variety of techniques have been proposed in the literature to overcome the limits imposed by this intrinsic absorption for graphene, which in turn restricts the modulation contrast of free space electro-optical modulators featuring the latter to a few percent in the absence of advanced accompanying optical structures [10]. We note that when employed in integrated wave-guided structures, the effective interaction length of light with graphene is no longer the thickness of a monolayer, but to a first approximation the length of the waveguide upon which graphene is integrated. Owing to this, high modulation contrasts may be achieved in the transmission regime ((T_{max}-T_{min})/T_{max}), ranging from 53% [11], 78% [12], 96% [13] when relying upon photon absorption to 99.9% [14] when exploiting phase shift in an interferometric configuration. Solutions envisaged to increase optical absorption have included the use of multilayer graphene

to enhance the number of passes of light through single graphene sheets [12,15,16] or, in the free-space configuration, exploiting resonant structures to confine optical energy in the vicinity of the graphene plane [17,18]. To date, the majority of such resonant structures have relied on the establishment of critically-coupled surface modes in one-dimensional gratings, yielding systems that are highly sensitive to absorption in graphene, and giving modulation contrasts approaching 100% [3,18]. The drawback of these devices is that they are highly wavelength-selective, giving full-width-at-half-maxima of a few nanometers for the reflected peaks subject to modulation, requiring redesigning of the underlying optical architecture in order to shift the operating wavelength. Furthermore, the resonant structures required to enhance the absorption in graphene are often complex, requiring sub-wavelength lateral features entailing multiple lithography and etching steps. Fabrication constraints for such lateral patterning can also lead to limited active areas of the resulting devices.

Over the past decade, the integration of graphene atop planar distributed Bragg reflectors (DBRs) has been proposed as a technologically simple way to enhance its interaction with light incident from free space while providing a spectrally broadband response. The wavelength range over which graphene's absorption is enhanced due to constructive interference of light at the DBR's surface depends on the bandwidth of the reflectance plateau, which may cover several hundreds of nanometers. In [19], by exploiting graphene's saturable absorption properties, graphene coated DBRs used to close resonant cavities provided a way to achieve mode-locking of pulsed lasers. Graphene topped DBR structures were later refined by modifying the thickness of the termination dielectric layer of the DBR in order to tune the optical absorption in graphene between 0 and ~10% at low laser powers, yielding a dynamic range of 5% absolute reflectance as a function of optical fluence (up to $100\mu J/cm^2$) [20]. More recent works integrating graphene onto DBRs have exploited the excitation of critically coupled Tamm plasmon polaritons (TPPs); propagating modes that exist between adjacent planar structures both displaying high reflectance, such as a metal-topped DBR in the near infrared domain [21] or a graphene-topped DBR in the terahertz frequency domain [22,23]. However, due to the necessity of phase-matching between free space radiation and the TPP, the fixed reflectance dip observed upon excitation is relatively narrow-band, whilst nevertheless displaying very high contrast with respect to the baseline reflectance (ΔR=80-100%).

In this work, a compromise is struck between modulation contrast and operating spectral bandwidth through the use of a double layer-graphene capacitor structure atop a broadband planar TiO_2/SiO_2 Bragg reflector for which the reflectance plateau is centered in the near infra-red telecommunications band (around $\lambda\sim1.55\mu m$). In this configuration, modulation contrasts in reflection of 20% or more for voltage swings of only +/−1V are observed over a ~250nm wavelength range, the centre of which can be adjusted by varying the angle of incidence. Through appropriate modeling, the measured reflectance spectra collected at different bias voltages allow us to infer the corresponding chemical potential in the two graphene sheets, which are shown to shift by up to 200meV. Our device design exploits a high work function oxide to induce a degree static doping of graphene (i.e. that in the absence of external bias), thereby reducing the voltage needed to shift the chemical potential of the graphene layers in the capacitor structure so as to render them transparent in the near infrared wavelength region of interest. The original use of a capacitor structure consisting of two parallel graphene electrodes separated by such an oxide also allows us to double the graphene induced optical absorption, which is further reinforced by the Bragg reflector, and increase the modulation contrast of our device.

We begin by describing the underlying Bragg reflector used in the experiment and its fabrication, followed by the elaboration of the double-layer graphene capacitor structure on the reflector surface. Having presented the associated reflectance measurements under free-space excitation in the near-IR for different external biases applied to the modulator device, we analyze our results using an opto-electrical model. This allows us to reproduce the absorption spectra of light by the

two graphene layers and deduce their corresponding chemical potentials, revealing the critical role played by the high work function oxide layer in our device performance.

2. Design and fabrication of the Bragg reflector and graphene double-layer capacitor

The design of our device is represented on Fig. 1(a). Simply described, it exploits a capacitor structure composed of two graphene layers that are transferred onto a Bragg reflector stack. The latter is composed of alternating quarter-wavelength thick high and low refractive index layers (here SiO_2/ TiO_2) so as to display a wideband reflectance plateau around the operation wavelength λ_B and concentrate optical intensity at the reflector's surface. Conditional upon terminating the Bragg reflector with the lowest refractive index material and interrogating it at normal incidence, the electric field amplitude at the surface of the reflector is doubled and the intensity quadrupled at λ_B, i.e. $I_{surf}(\lambda_B) = 4*I_0$ due to constructive interference between incoming and reflected waves. This constructive interference is harnessed here to enhance the absorption of photons in graphene transferred onto the surface of the reflector. However, terminating the Bragg mirror with a low refractive index layer partially sacrifices the reflectance plateau, leading to a dip in reflectance at the center wavelength (see Fig. 1(d)). We also note that the Bragg reflector response under grazing incidence is blue-shifted with respect to that at normal incidence, providing a way to adjust the device operation wavelength. Due to constraints linked to our reflectance measurement setup, we have here interrogated our device at an angle of incidence Θ=55° and have thus adjusted the required layer thicknesses of our target Bragg mirror structure to yield a reflectance plateau centered at 1.55µm telecom wavelengths at this angle. Under this off-normal interrogation, the surface intensity enhancement is slightly decreased though, giving a lower maximum value of around 3.5 times the incident intensity for an ideal Bragg reflector (see the grey line in Fig. 1(d)).

As will be evidenced in Section 4, an original feature of our modulator device is that it exploits static doping (i.e. that in the absence of an applied external bias) of graphene in order to reduce the switching voltage, and hence lower the energy consumption. Static doping consists here of shifting the chemical potential of graphene through the use of electron transfer to high work-function (ϕ) oxide layers, i.e. those for which the top of the conduction band lies energetically below the Dirac point of graphene (situated at 4.3eV below the vacuum level) as shown in Fig. 5(a), yielding p-doped graphene featuring holes below the Dirac point [24]. As shown on Fig. 1(a), our device thus includes the high work-function oxide WO_3, for which the theoretical work function is between 4.8 and 6.8eV according to the literature [25,26]. So as to ensure that the two graphene layers are in contact with the high work-function oxide material, WO_3 inclusions are placed both on the surface of the Bragg mirror below the graphene double-layer capacitor, as well as forming the interstitial dielectric layer in the capacitor enclosed by the two graphene layers, as shown in Figs. 1(a) and 1(c).

The surface optical intensity profile of our target Bragg mirror (with the reflectance plateau centered on 1.55µm) topped with 15nm of WO_3 (n=2.2) was calculated using a transfer matrix method (TMM) algorithm in s-polarization (as defined in Fig. 1(c)) and at an angle of incidence Θ=55°, to match our experimental conditions. The results are shown in Fig. 1(b) as a function of the depth within the mirror at the specific wavelength of 1.69µm. Figure 1(d) additionally shows the aforementioned (up to 3.5) surface intensity enhancement provided at the mirror surface as a function of wavelength along with the associated reflectance, which exhibits a characteristic dip in the middle of the reflectance plateau (at ~1.55µm wavelength), as discussed earlier. It has been verified through supplementary TMM calculations that variations in thickness between 0 and 30nm of the WO_3 layer on the Bragg mirror does not significantly change (within 3%) the maximum intensity enhancement at the surface; rather it red-shifts the wavelength at which the maximum occurs by up to 150nm. This red-shift is small enough to keep the wavelength of
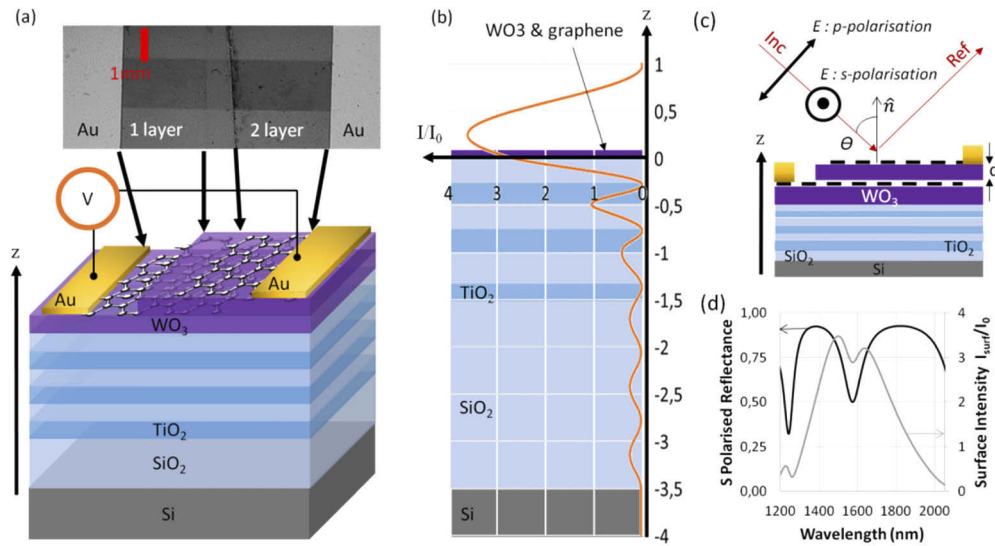
Fig. 1. (a) Perspective and (b,c) cross-section views of the capacitor structure on the Bragg reflector. Above (a) is an optical microscope image of the capacitor region, such that the plane of the image is in the plane of the graphene sheets. Shown on (b) is the vertical distribution of the optical intensity at λ=1.69 μm at Θ=55° for a Bragg mirror topped with 15 nm of WO_3. Also shown on (c), in which graphene is represented by the black dashed lines, are the electric field orientations for s- and p-polarizations, and the convention for measuring the angle of incidence Θ from the surface normal n. (d) Reflectance and normalized surface intensity for the target Bragg mirror structure, i.e. that for which the constituent layers have exactly $\lambda_B/(4n)$ thickness, for s-polarization at Θ=55°.

maximum surface intensity amplification comfortably within the high-reflectance plateau of the mirror, and is accounted for in the opto-electrical modeling detailed later.

We fabricated the Bragg reflector using the RF magnetron sputtering deposition technique in order to yield a thin film stack that is less prone to thermal stress when raised to the ~500°C required by the thermal annealing linked to the graphene transfer post-processing. The two materials deposited sequentially onto a commercially available silicon substrate with 2000nm of thermal oxide were SiO_2 (silica) and TiO_2 (titania), with refractive indices of 1.4 and 2.3 at the central operating wavelength of 1.55μm, with resulting target thicknesses of 270nm and 165nm respectively corresponding to $\lambda_B/(4n)$. Three alternations were deposited, as shown in Fig. 1. The actual thicknesses obtained were measured using spectroscopic ellipsometry at Θ=70° incidence and fitting of both refractive index dispersion and individual layer thicknesses in the 1000-2000nm wavelength range. The silica and titania were deposited by sputtering at room temperature from stoichiometric targets using an argon plasma at 2.10^{-3} mbar with oxygen compensation (3 sccm O_2 for silica, 4 sccm O_2 for titania). Forward powers of 150W (silica) and 370W (titania) yielded growth speeds of 5 and 3 nm/min respectively.

Following completion of the Bragg reflector, a thin film of 15nm nominal thickness of a WO_3 was deposited onto the surface. This and all subsequent WO_3 films were deposited by RF magnetron sputtering at room temperature from a stoichiometric oxide target using an argon plasma at 5.10^{-3} mbar with oxygen compensation (5sccm). A forward power of 100W yielded a growth speed of 4 nm/min.

Having completed the Bragg reflector and topped it with the high work function oxide, we begin the fabrication of the double-layer graphene capacitor on the surface. A first layer of graphene was transferred onto the reflector using the Trivial Transfer Graphene (TTG) product

from ACS Materials. TTG consists of 1*1cm squares of monolayer graphene supported on ~250nm of PMMA, and the transfer protocol involves floating the TTG in water, collecting it with the substrate (in this case the Bragg reflector/WO$_3$ stack) and removing the PMMA through a thermal annealing at 500°C in a tube furnace under 95% N$_2$ - 5% H$_2$ atmosphere lasting 3 hours. Following this first transfer, a part of the graphene sheet was shadow masked in order to provide a zone for the future (bottom) electrical contact. The deposition of WO$_3$ (nominal thickness 10nm) and graphene transfer steps were then repeated in order to create the double-layer graphene capacitor structure shown in Figs. 1(a) and 1(c). It should be noted that whilst TTG treated in this way gives satisfactory graphene coverage over a surface of several hundred square microns, or even up to a few square millimeters, a region of approximately 1mm*8mm – large enough to accommodate the measurement spot of our ellipsometry tool – was selected and masked using UV photolithography (AZ5214 photoresist deposited at approximately 1.3µm thickness). The un-masked regions surrounding the protected area were subjected to the following plasma treatments destined to strip the top graphene, interstitial WO$_3$, and bottom graphene respectively: oxygen plasma (100sccm O$_2$ flow, 100mT pressure, 50W power) for two minutes, SF6 plasma (50sccm flow, 100mT pressure, 200W power) for 1 minute, and again the oxygen plasma for 1 minute. Following this, the photoresist was stripped using acetone, and the whole structure was once again annealed in the same way during the graphene transfer processes for 1.5 hours. Finally, shadow masking was used to define a contact area on each graphene sheet, and a 150nm thick gold layer was deposited by electron beam assisted evaporation at a rate of 1-2Å/s, before wires were fixed using silver paste.

3.   Measurement of the electrically controlled graphene based optical reflector

3.1.   Optical measurements

Reflectance measurements were made in the wavelength window 1000-2000nm at $\Theta=55°$ incidence using our ellipsometry tool operating in photometric mode for the two linear polarization states p and s, indicated in Fig. 1(c). Note that the electric field is fully (partially) oriented in the plane of graphene for the s- (p-) polarization. A reference measurement was made on a double-side polished Si wafer in order to calculate the source power of the stabilized lamp, thereby allowing us to obtain the intensity reflectance coefficients R$_p$ and R$_s$. An initial reflectance measurement was made on a part of the Bragg mirror outside of the area of the graphene double-layer capacitor, shown by dashed lines in Figs. 2(a) and 2(b), and exhibited the spectral signature with the central dip that was simulated on Fig. 1(d). The device was then subjected to an external bias through the contact wires by grounding the lower graphene sheet and electrically polarizing the top one over the voltage range −1 to 1V. Reflectance spectra for both polarizations were collected for each bias voltage value, as shown in Figs. 2(a) and 2(b). We note that the electrically induced reflectance variation due to absorption in the graphene layers is highest at wavelengths where the surface intensity (grey curve on Fig. 2(a)) is maximized, and therefore reinforces the reflectance dip already situated at the center wavelength of the plateau. Furthermore, the variation is more visible for R$_s$ than R$_p$, because in s-polarization the electric field is entirely in the plane of the graphene sheets, whilst only a partial projection of the electric field is in this plane for p-polarization. This is further evidence, aside from the modulation of reflectance with applied bias, which the extinction of light in the device at around 1.55µm is due to absorption in the graphene.

The gross reflectance losses L induced by the graphene capacitor can be calculated as follows: $L_{gross,i}(\lambda) = R_{Bragg}(\lambda) - R_i(\lambda)$, where R$_{Bragg}$ is the reflectance of the bare Bragg reflector, R$_i$ the reflectance of the region featuring the capacitor structure, and the various bias values are indexed i, and is shown in Fig. 3(a). Figure 3(b) shows the reflectance contrast for all wavelengths $C_i(\lambda)=R_{s,i}(\lambda)–R_{s,−1V}(\lambda)]/R_{s,−1V}(\lambda)$, evidencing within the shaded region that a modulation contrast of more than 20% can be achieved over a 250nm wavelength range for voltage swings of
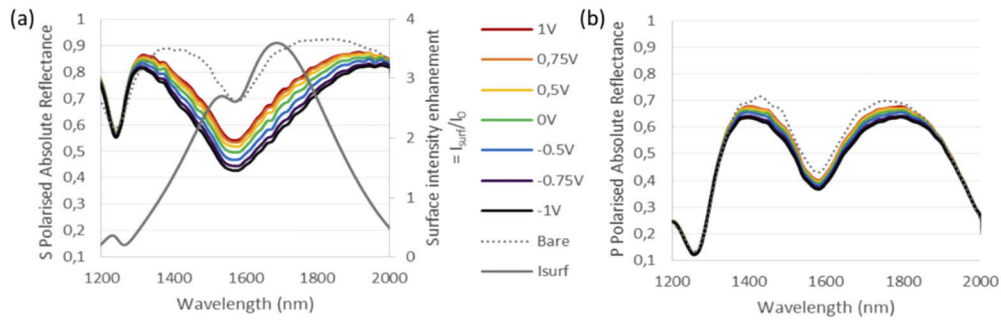
Fig. 2. (a) Measured s-polarised absolute reflectance (R_s) at $\Theta=55°$, around the Bragg mirror reflectance maximum for different applied voltages between −1 V and 1 V. Grey solid curve: Calculated surface intensity enhancement at the location of the bottom graphene layer for the same incidence angle and polarisation. Grey dashed curve: Reflectance of bare Bragg mirror (outside area of graphene capacitor structure). (b) Corresponding measured p-polarised absolute reflectance (R_p) spectra for the same range of applied bias.

+/−1V. We note that the maximum absorption variation achievable in each graphene sheet is equal to the net (single-pass, unit incident intensity) absorption of graphene of 2.3% multiplied by the local surface intensity, and is approximately equal to 7% where the surface intensity is maximized (i.e. $\geq 3*I_0$). This leads to a total maximum absorption modulation of 14% of the incident light, which corresponds to a maximum contrast of ~25% when the midpoint reflectance (i.e. the average over all biases) is around 50%, as is seen to be the case in Fig. 2(a) in the center of the reflectance plateau. In this paper, a balance has been struck between modulation contrast and spectral bandwidth, resulting in us quoting a contrast of 20% over a 250nm wavelength range.
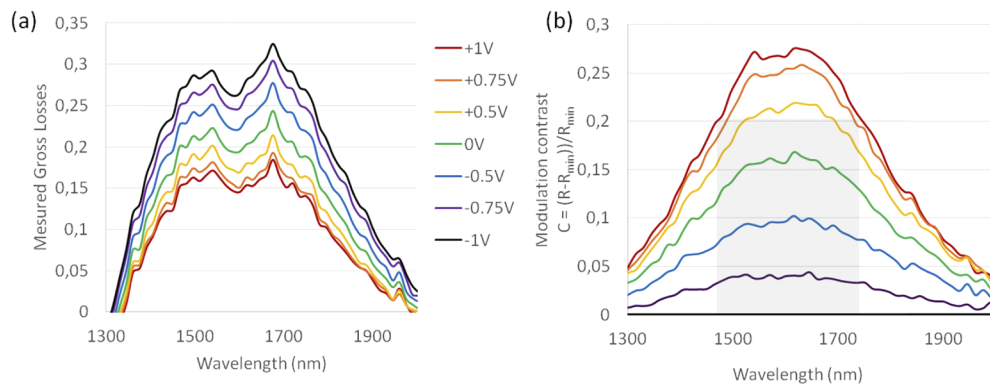

Fig. 3. For the s-polarization at θ=55° and as a function of the applied bias: (a) measured gross losses for all applied biases, (b) measured reflectance contrast relative to the reflectance at −1 V bias.

3.2. DC electrical measurements

Although roughly providing the intended capacitor-like electrical behavior, we note that a small leakage current was measured across the device when applying different bias voltages. We exploit this additional electrical measurement in a supplementary analysis included in the Appendix, so as to model the operation of our device and further confirm the relevant values of graphene chemical potentials that are key to account for the device's low voltage operation. To this aim, a

finer sweep of applied bias voltages, in steps of 100mV, was made between −1 and 1V in order to collect the leakage current through the capacitor device more accurately. The measured current is shown in Fig. 8(d).

3.3. Electro-optic modulation bandwidth measurement

In order to establish the maximal operating frequency of our device, we have performed frequency-resolved modulation response measurements at 1.64μm wavelength at normal incidence. The device was connected to a waveform generator and the frequency swept across the kHz – MHz range, with excitation and collection from monomode optical fibers. The reflected signal was detected using a cathode grounded photodiode and the electrical output connected to a digital oscilloscope. Figure 4 shows the frequency response of the modulator, and allows the 3dB bandwidth of 0.9 MHz to be determined. This of the same order of magnitude as the theoretical value, taking into account the dimensions of the double-layer graphene capacitor, whose area is estimated as being around 1mm^2 over which the two graphene sheets overlap. We calculate the capacitance $C = \varepsilon_0\varepsilon_d A_c/d = 4.4$nF ($\varepsilon_0$ is the free space permittivity, ε_d the relative dielectric constant of WO$_3$ at low frequency (4.48), A$_c$ the capacitor surface area (1mm^2), and d the oxide layer thickness). Therefore, we estimate the high frequency cutoff $f_{max} = 1/(2\pi RC) = 0.2$ MHz, assuming a resistance R=200Ω dominated by graphene's sheet resistance (approximately 200 Ω/□ far from the Dirac point [12]).
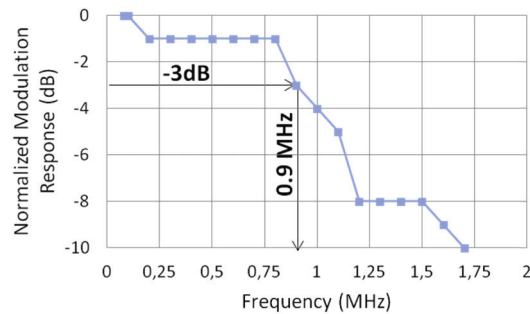

Fig. 4. Frequency resolved modulation response (normalized to maximum value at 0.1 MHz), show 3 dB bandwidth of 0.9 MHz.

Whilst we note that this upper frequency limit is somewhat lower than those reported for other graphene-based optical modulators in the literature (discussed in more detail in Section 5), we note that it is directly linked to the device's surface area. In our case, the device was intentionally fabricated on the millimeter scale to allow us to probe it with our ellipsometry tool, for which the spot size is of this order of magnitude. Typical surface areas for free-space modulators are around 100 μm^2 (i.e. dimensions of 10μm*10μm) [27]. Given the planar geometry of our device architecture, standard UV optical lithography techniques may be used to delimit regions of this size and plasma etching used to remove the surrounding excess device structure in the substrate (lateral) plane. If the active surface area were reduced laterally to 100 μm^2 (i.e. a reduction of a factor of around 10,000), the expected bandwidth would be around 10 GHz assuming no consequential contact resistance, demonstrating the pertinence of the vertical architecture of our device.

4. Opto-electrical modeling

The goal of the modeling presented here is to analyze the electro-optical operation of our device, and theoretically reproduce the measured signature so as to extract, in particular, the chemical potentials ($\mu_{1,2}$) of the graphene sheets in the polarized capacitor structure. We proceed by

undertaking a joint modeling of (i) the optical absorption in the graphene sheets, accounting for the spectral dependence of the absorption as a function of the device geometry and the chemical potential of the graphene sheets, coupled with (ii) the relation for the electric field present in the capacitor, thereby ensuring that the resulting chemical potentials together with the field imposed by the external bias allow for electrostatic equilibrium in the device. This joint model allows us to reproduce the experimentally obtained gross loss spectra to infer the chemical potentials. In the Appendix, a confirmatory electrical modeling step to reproduce the leakage current through the capacitor device as a function of the chemical potentials of the graphene electrodes is carried out.

4.1. Optical modeling

Optical absorption in graphene is defined by the real part of its surface conductivity (or imaginary part of its effective dielectric constant), defined through the well-known Kubo formula [28]. Examination of the real part of the surface conductivity, dominated by loss-inducing inter-band electron transitions, shows that it can be approximated to a Fermi-Dirac-like function, with the spectral position λ_s of the step determining the onset of absorption defined by the chemical potential μ via $\lambda_s = hc/(2\mu)$, and the width of the step indicating the finite possibility of (de-)population of states (below) above the Fermi level defined by $2k_BT$, with k_B Boltzmann's constant and T the temperature. Finally, it is known that the optical absorption for a single passage of light through graphene is 2.3% for photons possessing energies well above twice the chemical potential. These facts lead to the following simple model for the net optical absorption coefficient for graphene (in single-pass, unit incident intensity configuration), for which the only variable is the chemical potential μ, that has been tested against absorption spectra calculated through rigorous application of the Kubo formula:

$$A_{net}(\lambda) = 0.023 * \left(1 - \frac{1}{\exp\left[\frac{hc/\lambda - 2\mu}{2k_BT} + 1 \right]} \right) \tag{1}$$

Another contribution to diminished reflected intensity from the system is scattered optical losses, mainly due to impurities remaining on the surface of the graphene from the wet transfer process, which are considered wavelength independent. We note that the gross losses due to absorption in the graphene and scattering are simply the net losses for these two processes multiplied by the surface intensity at the graphene location. Therefore, to calculate the gross losses induced by the graphene capacitor for each bias voltage, we need to evaluate the net absorption $A_{net,i}$ in each graphene sheet (top and bottom), add on the scattering losses S (a fit parameter), and multiply by the intensity at the respective vertical location of the top and bottom graphene layer:

$$L_{gross,i}(\lambda) = [A_{net,top,i}(\lambda) + S]I_{surf,top}(\lambda) + [A_{net,bottom,i}(\lambda) + S]I_{surf,bottom}(\lambda) \tag{2}$$

The spectral dependence of L_{gross} is calculated using this formula and compared with the experimentally obtained value during the fitting process described later. The surface intensities at the vertical positions corresponding to the graphene sheets are very sensitive to the WO_3 thicknesses separating the graphene from the Bragg reflector surface, and for the top graphene sheet can vary by a factor of 2 at a given wavelength over the range of interstitial oxide thicknesses that we consider, spanning from 0 to 30nm (meaning that the gross losses in the top graphene sheet can vary by this same factor). Whilst the bottom graphene layer is considered to be placed on a WO_3 layer of 15nm thickness, the surface intensity for the top graphene sheet is recalculated (using a combined TMM and linear interpolation method) for all interstitial oxide layer thicknesses tested during the fit process.

4.2. Electrostatic modeling

As stated earlier, upon contact with a high work-function oxide, transfer of electrons occurs from below the Dirac point of graphene into the conduction band of the oxide. A negligibly thin space-charge region is formed, shaded grey in Fig. 5(c) in which its thickness is exaggerated for representational purposes, which manifests through a bending of the oxide conduction and valence bands towards the interface with the graphene. As will be detailed in the Appendix, the space-charge layer thickness can be thought of equivalently as a percentage of groups in the surface layer of oxide in contact with the graphene having accepted an electron. The addition of the top layer of graphene to form the double-layer capacitor structure enclosing a layer of WO_3 leads to a repeat of the electron transfer phenomenon previously described, resulting in a space-charge region on both sides of the WO_3 and yielding identical shifts in the chemical potentials of both the top (μ_1) and bottom (μ_2) graphene sheets, as shown in Fig. 5(d).
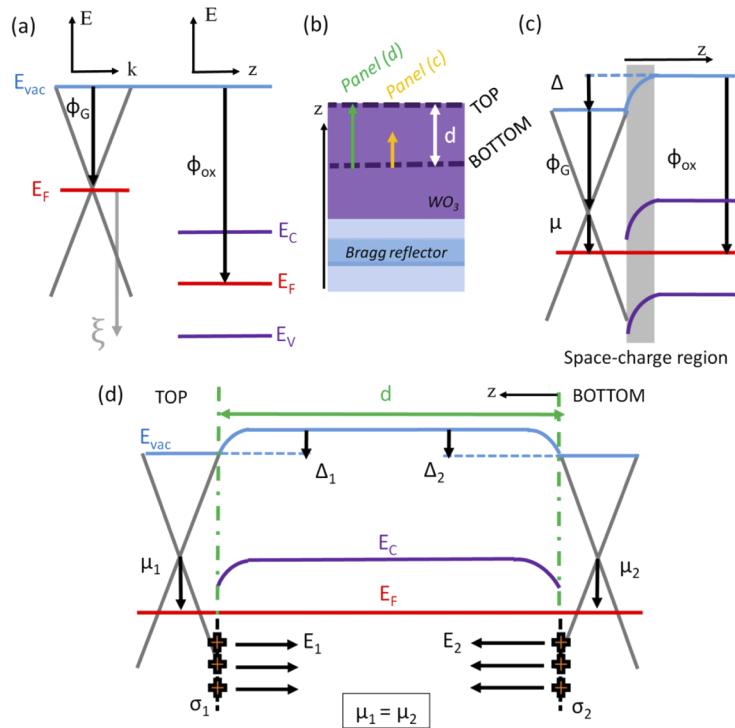

Fig. 5. Schematic band diagrams for (a) out-of-contact graphene (simplification around Dirac point) and high work function oxide. (b) Schematic of the double layer graphene capacitor atop the Bragg mirror, with orange/green arrow showing the spatial extent of the band diagram shown in panel (c/d). Band diagrams at the equilibrium for (c) in-contact graphene and oxide junction (d) double-layer graphene capacitor. Note that the bands for graphene (grey) are in energy-momentum space, whilst those for the oxide are in energy-position (depth, z) space.

We now consider the capacitor device under external bias. In order to calculate the shift in the graphene chemical potentials due to the applied voltage, we construct a simple model for a parallel plate capacitor, for which the plates correspond to the two graphene sheets. The overall expression governing the static electric field present in the structure is the following:

$$E_{ap} = E_1 - E_2 + E_{int} \tag{3}$$

where E_{ap} is the field induced by the applied bias, $E_{1,2}$ are the fields radiated by the planes of charges gathered on the top and bottom graphene sheets respectively, and E_{int} the field corresponding to the difference in Fermi levels across the WO_3 dielectric separating the graphene sheets.

As is shown Appendix B, this expression can be developed to yield:

$$\frac{V_a}{d} = \left[\frac{eD_0}{2A\varepsilon_0}\right](\text{sgn}(\mu_1)\mu_1^2 - \text{sgn}(\mu_2)\mu_2^2) - \frac{(\mu_1 - \mu_2)\varepsilon_d}{d} \qquad (4)$$

where V_a is the applied bias, d the thickness of the WO_3 separating the graphene sheets, e the elementary charge, D_0=0.102 states/eV is the density of states per graphene lattice unit cell and A=5.18×10^{-20} m^2 the unit cell area, ε_0 the free space permittivity, ε_d the relative dielectric constant of WO_3 at zero frequency (equal to 4.48).

Equation (4) does not permit us to calculate definite values for each of μ_1 and μ_2, rather we can find coupled pairs of chemical potentials that satisfy it for a given applied bias. Such coupled pairs can be represented by a series of points in μ_1,μ_2 space forming continuous loci, with each locus of points representing a bias voltage for which the pairs are allowed, such as those in Fig. 6(a). There are essentially two behaviors manifesting themselves in different regions of the parameter space, as a function of their proximity to the origin where $\mu_1=\mu_2=0$ (i.e. zero field radiated from the graphene sheets) for which the Fermi levels are both at the charge neutrality (Dirac) points: (i) close to the origin, the radiated fields from the graphene sheets are low compared with the field induced by the applied bias. For non-zero values of the latter, the allowed μ_1,μ_2 pairs are dissymmetric (i.e. μ_1 is very different to μ_2) so that one of the graphene sheets may divest itself of charges and radiate a field to cancel the applied bias field. (ii) Far from the origin, the radiated fields from the graphene sheets are far stronger than the applied bias-induced field for the range of applied voltages considered. As such, the loci of allowed pairs tends towards $\mu_2=\mu_1$ such that the radiated fields (which are opposite in direction) may cancel.

4.3. Fitting of experimental gross optical losses

To analyze our results using the electro-optical model described above, we follow the following fitting procedure: parameters to be fit are the exact thickness *d* of the interstitial WO_3 layer and the scattering coefficient *S*. These parameters are swept across predefined ranges, shown on the axes of the fit merit parameter *M* in Fig. 6(b). For each value of *d*, the loci of allowed μ_1 and μ_2 pairs are calculated for each applied bias. For each pair, the absorption in the two graphene sheets is calculated through Eq. (1) (dependent on $\mu_{1,2}$), and the overall gross losses are calculated for all applied biases with Eq. (2) (dependent on *S* and *d*, the latter for calculating the optical intensity on the top graphene sheet). These theoretical loss curves are then compared to the experimental loss measurements shown in Fig. 3(a) through least-squares parameters χ_i, and the best pair of chemical potentials (i.e. that minimizing χ) for each applied bias is used to calculate the fit merit parameter $M = \Sigma(\chi_i)$. As can be seen from the minimum in Fig. 6(b), the thickness of the interstitial WO_3, *d*, is found to be 12.5nm (i.e. relatively close to the 10nm nominal value), and a relatively low graphene defect induced light scattering coefficient of 2.4% is found optimum. Figure 6(c) shows the comparison between the gross losses extracted from the optical measurements and those calculated for all applied biases in this best fit situation, and Fig. 6(d) shows the corresponding chemical potentials of the two graphene sheets. Finally, Fig. 6(e) shows the net (single-pass, unit incident intensity) absorption spectra for the two graphene sheets, revealing that the absorption edge in the absence of applied bias is centered within the wavelength range considered due to the static doping conferred by the high work-function oxide. In effect, the doping level at zero bias is around 0.4 eV, which is around 100-200 meV higher than expected for graphene on an 'inert' dielectric or semiconductor substrate [29], showing the effective static doping role of the WO_3 oxide layer. Under bias we note, unsurprisingly, that it is the top graphene
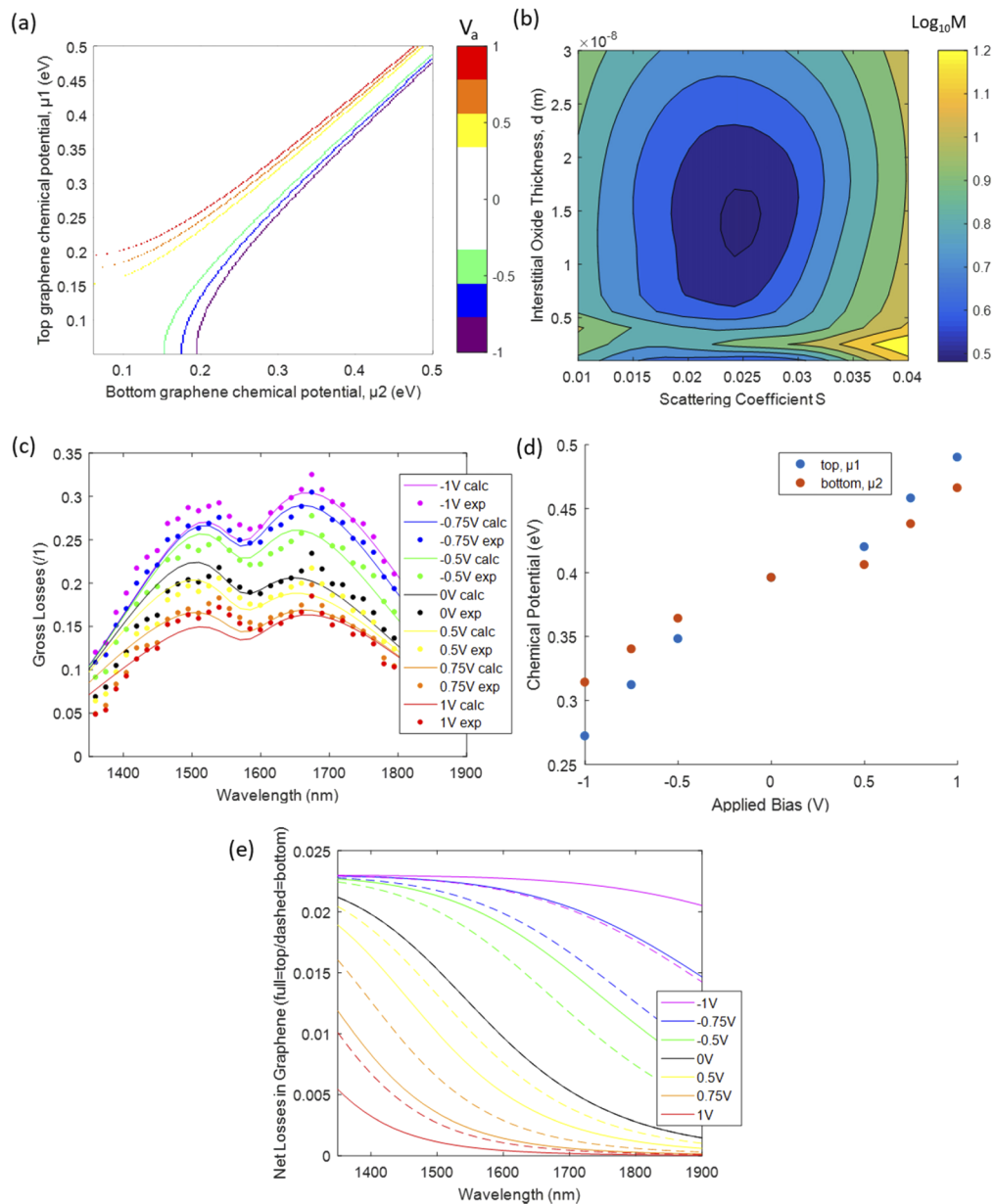
Fig. 6. (a) Loci of allowed μ_1, μ_2 pairs for d=12.5 nm, separate colored points for each non-zero applied bias voltage V_a. (b) Merit parameter M (blue = minimum) as a function of the fitting parameters, i.e. the dielectric thickness d and scattering coefficient S, showing optimum at d=12.5 nm and S=2.4%. (c) Spectra of measured and simulated gross losses for d=12.5 nm, S=2.4% and best μ_1, μ_2 pairs for all applied bias voltages. (d) Best fit values of μ_1 (top graphene sheet) and μ_2 (bottom graphene sheet) as a function of bias voltage V_a. (e) Net (single-pass) absorption losses in each graphene sheet (solid line for top graphene, and dashed line for the bottom graphene) for all applied bias voltages.

layer (associated with μ_1) that displays the greatest shifts in chemical potential, whilst that of the lower layer also shifts from its initial position but to a lesser degree. The underlying band diagrams in the capacitor device under external bias, and the charge transfer mechanisms leading to their establishment, are discussed in Appendix C.

5. Discussion

The device described in this work presents three main features that contribute towards its broadband and low voltage operation, and whose association gives rise to the novelty of this work: (i) the use of a Bragg mirror featuring a spectrally large reflectance plateau and allowing for enhancement of optical intensity in the planes of the graphene sheets. Although its use was demonstrated here for off-normal incidence, we note that even better modulation contrast than currently reported could be achieved if illuminated under normal incidence. (ii) The integration of a double-layer graphene capacitor structure allows for increased absorption in two graphene sheets, thereby improving the modulation contrast. (iii) A high work-function oxide is exploited to statically tune the chemical potential of graphene in the absence of an external bias, placing the graphene's spectral absorption edge at near infrared telecom wavelengths and reducing the required bias to render it fully absorbing or transparent.

To place the performance of our device into context, recent near infrared electro-optic modulators exploiting absorption in graphene and displaying operating spectral bandwidths $\Delta\lambda > 100$nm have demonstrated lower modulation contrasts of the order of C=3% at 1.55μm [10] due to the absence of advanced adjacent structures designed to assist optical absorption in graphene. Our device builds on this work by using the underlying Bragg mirror to enhance the light-graphene interaction to display a maximum contrast C=25%. By way of comparison between our work and others using planar Bragg mirrors to enhance absorption in graphene, we may consider the afore cited works on Tamm plasmon polaritons [21,22,23]. We remind the reader that TPPs, as propagating surface modes, give rise to extremely high concentrations of optical energy in a single plane of the structure in which graphene may be situated. This leads to very high reflectance contrasts (ΔR=80-100%) between wavelengths inside the TPP induced reflectance dip and outside. However, the constraint implied by exploiting a propagating surface mode to attenuate light is that radiation from free space must be phase matched to the propagation constant of the TPP, leading to relatively narrow-band reflectance dips with quality factors of 10-100. This would limit the operating spectral bandwidth of a modulator relying on TPP excitation at a center wavelength of 1.55μm to $\Delta\lambda \approx$ 15-150nm over which the modulation contrast could exceed half its maximum value. By way of comparison, as can be inferred from Fig. 3(b), the equivalent metric for our device would be $\Delta\lambda \approx$ 400nm.

The low switching voltages of our device – spanning a 2V range and shifting the chemical potential of graphene by 0.2eV – can be appreciated when comparing them to reported values in the literature for other modulator structures employing solid-state charge injection gating. References [30,31] demonstrate graphene-based free space electro-optic modulators operating in reflectance configurations in the THz frequency domain, for which the chemical potential of the graphene is varied over 0.4eV using drive voltage swings of 24V on the one hand, and over 0.25eV using voltages swings of 60V on the other. It should nevertheless be noted that identical switching voltage ranges to those that we report have been cited in [18] for a near infrared modulator using an ion gel solution to exchange charges with the graphene layer, whilst underlining the integration challenges that the use of ion gels can present. We may also compare our switching voltages for the quoted 20% modulation contrast over a 250nm wavelength range with those necessary to achieve the same degree of modulation in waveguide based modulators; our value of 2V is near identical to those in [11,12] for an operating wavelength of ≈1.53μm, whilst for [13] in order to require the same range of switching voltage the central value must be tens of volts (note that the switching energy scales linearly with the central value).

Finally, we compare the maximum operating frequency $f_{max} = 0.9$ MHz of our device to those in the literature. As already stated f_{max} is inversely proportional to a capacitor structure's surface area, and we take as a reference area for industry ready devices $100\mu m^2$ at which we estimate our device would operate at around 10 GHz with low resistance contacts. References [12,13], also employing double layer graphene capacitor structures covering (i) on the one hand $40\mu m$ of an optical waveguide and of width $2\mu m$ (i.e. an area close to our reference value of $100\mu m^2$) and (ii) on the other $30\mu m$ of a waveguide and of width $1.5\mu m$ (i.e. an area of half of our reference value), demonstrate f_{max} values of (i) 1 GHz and (ii) 30 GHz. In the latter case (ii), it is the much higher thickness of the interstitial oxide layer separating the two graphene sheets of 65nm that explains the sharp increase in modulation bandwidth. However, as has been shown in the previous paragraph, the central switching voltage value for the device in question is ten times higher, with consequential scaling of the switching energy and hence power consumption.

6. Conclusion

In this work, we have demonstrated low voltage near-infrared electrically tunable graphene based Bragg mirrors at telecom wavelengths. Our device allows for contrasts in absolute reflection of 20% or more over a 250nm wavelength range centered in the near-infrared telecom band, and maximum contrasts of 25% when interrogated at oblique incidence. The underlying planar Bragg reflectors enhance the optical absorption in graphene over a wide spectral range, achieving absorptions of $\approx$7% of incident photons per graphene sheet (so $\approx$14% in total). The use of a double-layer graphene capacitor structure and low bias voltages ranging between +/−1V have been shown to allow for the tuning of graphene's Fermi level over a 200meV range, centered on 400meV. The low voltage required for the device operation was enabled by our original use of a high-work function oxide layer, effectively providing a static doping of the graphene sheets. The device is suitable for use as a free-space wideband electro-optic modulator, for which the central operating wavelength can be readily adjusted by changing the incidence angle.

Appendix A: development of the electrostatic model for the capacitor structure

Equation (3) may be developed as follows, taking the chemical potentials of the two graphene sheets $\mu_{1,2}$ to be positive when the graphene Fermi level is below the Dirac point (and hence representing a build-up of positive charges due to evacuation of electrons from the corresponding graphene sheet, i.e. hole- or p-doping) :

$$\frac{V_a}{d} = \frac{\sigma_1}{\varepsilon_0} - \frac{\sigma_2}{\varepsilon_0} - \frac{(\mu_1 - \mu_2)\varepsilon_d}{d} \tag{5}$$

where V_a is the applied bias, σ_1 and σ_2 are the surface charge density of the top and bottom graphene sheet respectively, ε_0 the free space permittivity, d the thickness of the WO_3 separating the graphene sheets and ε_d its relative dielectric constant at zero frequency and equal to 4.48.

We then use the following relationship to link the surface charge density σ to the chemical potential in graphene, through integrating the areal density of states (itself a linear function of energy) from the Dirac point up to the Fermi level:

$$\sigma = e \int_0^\mu D(\xi)d\xi = e \int_0^\mu \frac{|\xi|D_0}{A}d\xi = \text{sgn}(\mu)\frac{eD_0}{2A}\mu^2 \tag{6}$$

where e is the elementary charge, D_0=0.102 states/eV is the density of states per graphene lattice unit cell and $A=5.18\times 10^{-20}$ m^2 the unit cell area.

Substituting this expression into Eq. (5) gives the final equation linking the respective chemical potentials of the two graphene sheets to the applied bias, Eq. (4).

Appendix B: band diagrams of capacitor structure under external bias

Figure 7 shows representations of the supposed band diagram of the system at maximum bias (+/- 1V), referenced to the Fermi level of the lower metal contact that is grounded. At zero bias, the charge transfer of electrons from the graphene to the conduction band of the WO_3 leads to a bending of the oxide band edges such that they fall to the system's Fermi level, indicating that the conduction band is partially occupied in a space-charge layer adjacent to each graphene sheet. Upon application of an applied bias, the Fermi level of the metal contacting the top sheet of graphene shifts directly following the voltage (i.e. 1V bias = 1eV shift) and the equilibrium across the device is broken. The application of a negative bias injects electrons into the upper graphene sheet (reducing the chemical potential), whilst the deformation of the band diagram and namely the potential gradient across the oxide leads to electron transfer from the oxide back into the bottom graphene. This raises the Fermi level of the lower graphene sheet also, though to a lesser extent, and reduces the depth of the adjacent space-charge layer (shaded in grey in Fig. 7). For positive biases, the inverse occurs: charges are extracted from the upper graphene sheet directly, whilst a lower number of electrons are transferred to the oxide from the bottom graphene, leading to an increase in the chemical potentials of both sheets. The effective thickness of the space-charge layer adjacent to the bottom graphene sheet is thereby increased to accommodate the extra charges. Electron transfer necessary for the formation of the equilibrium states shown is schematized in Fig. 7 with green arrows, for which the thickness roughly indicates the number of electrons displaced. The leakage current between the top (bottom) graphene sheet and the oxide in the case of positive (negative) bias is discussed in Appendix C.
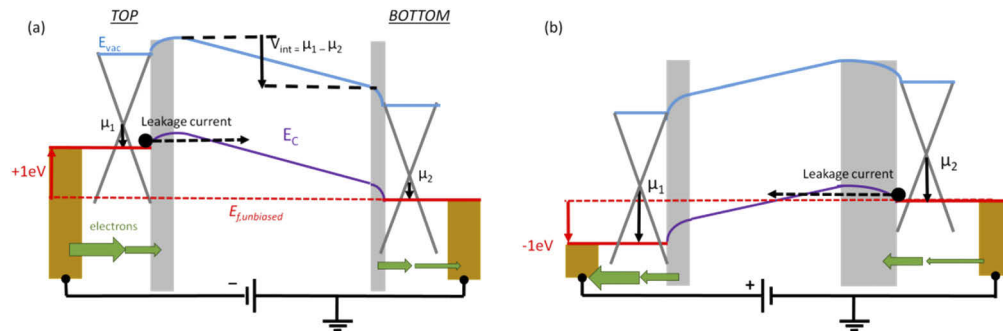

Fig. 7. Schematic band diagram of contacted double-layer graphene capacitor under (a) negative, (b) positive bias voltages applied to the top graphene sheet, where the horizontal axis between the two graphene sheets represents depth within the interstitial oxide. Grey shaded areas represent the space-charge regions.

For all chemical potentials, the space-charge layer occupies a negligibly small thickness of the overall oxide layer, justifying the use of a common oxide thickness over which V_{int} (=μ_1-μ_2) acts for all chemical potentials. Indeed, taking into account the maximum surface charge density of graphene encountered in our experiment, corresponding to a chemical potential of 0.5eV, which can be calculated (through use of Eq. (6) and dividing by the elementary charge) as being around 3.5×10^{17} electrons/m^2 donated to the oxide, accounting for the density and molar mass of WO_3 only around 5% of the stoichiometric WO_3 groupings in the very surface layer of the oxide would receive a single electron. It is for this reason that the space-charge layer thickness can be thought of equivalently as a percentage of groups in the surface layer of oxide in contact with the graphene having accepted an electron.

Appendix C: leakage current modeling

The voltage-current characteristics of the capacitor device under applied bias, represented by the points at 0.1V intervals in Fig. 8(d), may be used to confirm the trend in the chemical potential variation for the graphene sheets, calculated previously from the optical measurements. In order to do this, whilst reminding that the device shows principally the capacitor behavior intended, we acknowledge that we must consider a small leakage current caused by pinhole defects in the interstitial oxide layer, which occurs for both polarizations (i.e. signs of V_a).
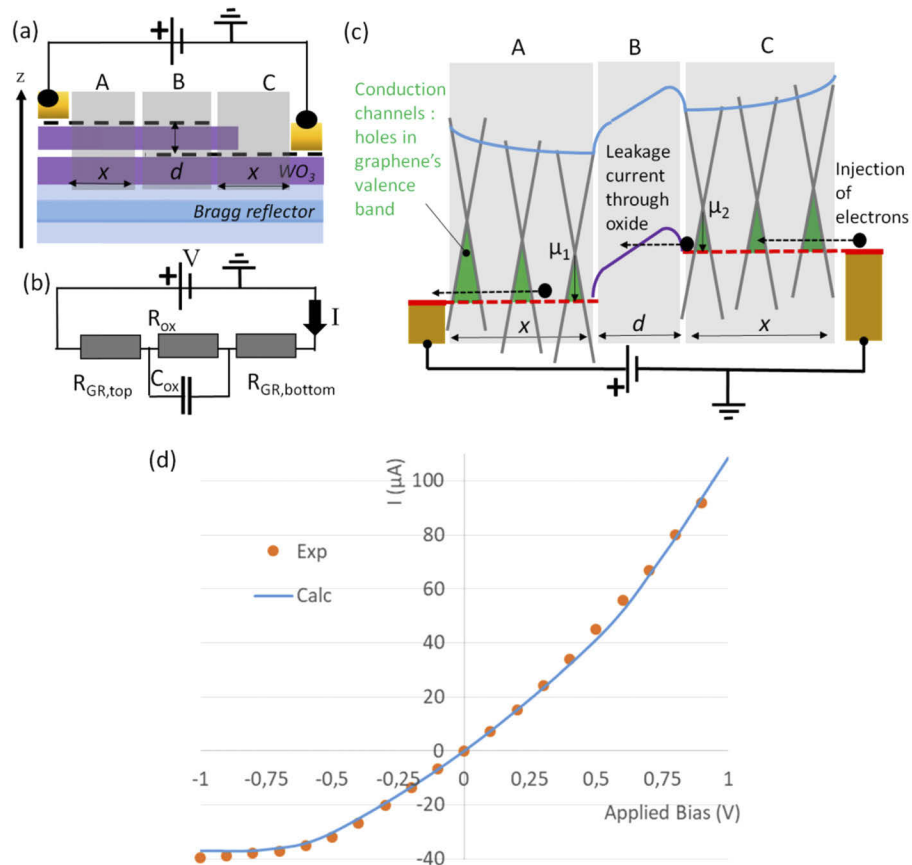

Fig. 8. (a) Cross section of double-layer graphene capacitor on Bragg reflector, showing regions A, B, and C referred to in (c). (b) Equivalent circuit diagram for the device. (c) Band diagram under positive applied bias. In region B, the horizontal axis of corresponds to the depth within the oxide, whilst in regions A and C it corresponds to the distance from the top and bottom electrodes respectively. The spatial evolution of the chemical potential for the top graphene sheet as a function of distance from the top electrode, as reported in the literature [32], is evident in regions A and C. The conduction channels available, i.e. holes in graphene's valence band through which injected electrons may hop, are shown in green. (d) Measured and calculated current as a function of applied bias.

The conductance of the graphene sheets that serve as the parallel plates of the capacitor device and carry electrons from the metal electrodes to the active area (where the two sheets are stacked) is directly governed by the number of available charge carriers - i.e. holes in the graphene valence bands through which electrons injected at the electrodes may hop - which is in turn given through integrating the density of states below the Dirac point down to the Fermi level for each sheet, as

in Eq. (6). This is represented in Fig. 8(c), where the areas of the green shaded sections represent the number of available states for conduction of injected electrons. In practice, we suppose that the lowest chemical potential for each sheet, giving the limit of the conductance, occurs in the center of the device (i.e. farthest from the metal electrodes) and is therefore that calculated through the optical measurements presented previously. The lateral separation - that is, in the plane of the graphene sheets - between the optically probed active area and the metal contacts of a few millimeters leads to a gradient in the chemical potential on the graphene, as suggested in Ref. [32]. We can therefore resume the conductance of each graphene sheet as being proportional to the square of the lowest chemical potential experienced by each sheet:

$$G_{GR,top/bottom} = k.\mu_{1/2}{}^2$$

(7)

where k is a proportionality constant.

The device is represented as a simplified equivalent circuit, shown in Fig. 8(b), composed of two resistances for the top and bottom graphene sheets, $R_{GR,top}$ and $R_{GR,bottom}$, and a capacitance C_{ox} and a resistance R_{ox} in parallel for the oxide layer. We note that in the DC measurement regime considered, the contribution of the capacitance to the total impedance of the oxide layer is null. The resistances may alternatively be expressed as conductances, such that the total conductance G_{tot} may be written:

$$G_{tot} = \frac{1}{\frac{1}{G_{GR,top}} + R_{ox} + \frac{1}{G_{GR,bottom}}}$$

(8)

The resulting total conductance, calculated through Eq. (8), can be used to calculate a theoretical current flow through the device via the relation $I = G_{tot}.V_a$. Fitting the proportionality constant k and the fixed resistance of the oxide layer allows us to accurately reproduce the experimentally measured current using the chemical potentials found previously, as shown by the solid line in Fig. 8(d), lending further proof of their validity. We note that the reduced current magnitude for negative applied bias voltages reflects the low chemical potential of the two graphene sheets in this case, thereby reducing the number of available conduction channels.

Disclosures

The authors declare no conflicts of interest.

References

1. F. Bonaccorso, Z. Sun, T. Hasan, and A. C. Ferrari, "Graphene photonics and optoelectronics," Nat. Photonics **4**(9), 611–622 (2010).
2. J. T. Kim, J.-H. Choe, J.-S. Kim, D. Seo, Y. D. Kim, and K. H. Chung, "Graphene-based plasmonic waveguide devices for electronic-photonic integrated circuit," Opt. Laser Technol. **106**, 76–86 (2018).
3. A. Majumdar, J. Kim, J. Vuckovic, and F. Wang, "Graphene for Tunable Nanophotonic Resonators," IEEE J. Sel. Top. Quantum Electron. **20**(1), 68–71 (2014).

4. V. Sorianello, M. Midrio, G. Contestabile, I. Asselberghs, J. Van Campenhout, C. Huyghebaert, I. Goykhman, A. K. Ott, A. C. Ferrari, and M. Romagnoli, "Graphene–silicon phase modulators with gigahertz bandwidth," Nat. Photonics **12**(1), 40–44 (2018).

5. F. Javier Garcia de Abajo, "Graphene Plasmonics: Challenges and Opportunities," ACS Photonics **1**(3), 135–152 (2014).

6. T. Wood, M. Kemiche, J. Lhuillier, P. Demongodin, B. Vilquin, P. Rojo-Romeo, A. Benamrouche, P. Régrény, S. Callard, X. Letartre, and C. Monat, "Towards low-power near-infrared modulators operating at telecom wavelengths: when graphene plasmons frustrate their metallic counterparts," J. Opt. Soc. Am. B **37**(5), 1563–1576 (2020).

7. P. Demongodin, H. El Dirani, J. Lhuillier, R. Crochemore, M. Kemiche, T. Wood, S. Callard, P. Rojo-Romeo, C. Sciancalepore, C. Grillet, and C. Monat, "Ultrafast saturable absorption dynamics in hybrid graphene/Si3N4 waveguides," APL Photonics **4**(7), 076102 (2019).

8. M. Mohsin, D. Schall, M. Otto, B. Chmielak, C. Porschatis, J. Bolten, and D. Neumaier, "Graphene based on-chip variable optical attenuator operating at 855 nm wavelength," Opt. Express **25**(25), 31660 (2017).

9. H. Li, Y. Anugrah, S. J. Koestera, and M. Li, "Optical absorption in graphene integrated on silicon waveguides," Appl. Phys. Lett. **101**(11), 111110 (2012).

10. D. Aznakayeva, F. Rodriguez, O. Marshall, and A. Grigorenko, "Graphene light modulators working at near infrared wavelengths," Opt. Express **25**(9), 10255–10260 (2017).

11. M. Liu, X. Yin, E. Ulin-Avila, B. Geng, T. Zentgraf, L. Ju, F. Wang, and X. Zhang, "A graphene-based broadband optical modulator," Nature **474**(7349), 64–67 (2011).

12. M. Liu, X. Yin, and X. Zhang, "Double-Layer Graphene Optical Modulator," Nano Lett. **12**(3), 1482–1485 (2012).

13. C. Phare, Y.-H. Lee, J. Cardenas, and M. Lipson, "Graphene electro-optic modulator with 30 GHz bandwidth," Nat. Photonics **9**(8), 511–514 (2015).

14. V. Sorianello, M. Midrio, G. Contestabile, I. Asselberghs, J. Van Campenhout, C. Huyghebaert, I. Goykhman, A. K. Ott, A. C. Ferrari, and M. Romagnoli, "Graphene–silicon phase modulators with gigahertz bandwidth," Nat. Photonics **12**(1), 40–44 (2018).

15. S. Koestera and M. Li, "High-speed waveguide-coupled graphene-on-graphene optical modulators," Appl. Phys. Lett. **100**(17), 171107 (2012).

16. Z. Sun, A. Martinez, and F. Wang, "Optical modulators with 2D layered materials," Nat. Photonics **10**(4), 227–238 (2016).

17. G. Sui, J. Wu, Y. Zhang, C. Yin, and X. Gao, "Microcavity-integrated graphene waveguide: a reconfigurable electro-optical attenuator and switch," Sci. Rep. **8**(1), 12445 (2018).

18. T. Sun, J. Kim, J. M. Yuk, A. Zettl, F. Wang, and C. Chang-Hasnain, "Surface-normal electro-optic spatial light modulator using graphene integrated on a high-contrast grating resonator," Opt. Express **24**(23), 26035–26043 (2016).

19. J.-L. Xu, X.-L. Li, Y.-Z. Wu, X.-P. Hao, J.-L. He, and K.-J. Yang, "Graphene saturable absorber mirror for ultra-fast-pulse solid-state laser," Opt. Lett. **36**(10), 1948–1950 (2011).

20. C. A. Zaugg, Z. Sun, V. J. Wittwer, D. Popa, S. Milana, T. S. Kulmala, R. S. Sundaram, M. Mangold, O. D. Sieber, M. Golling, Y. Lee, J. H. Ahn, A. C. Ferrari, and U. Keller, "Ultrafast and widely tuneable vertical-external-cavity surface-emitting laser, mode-locked by a graphene-integrated distributed Bragg reflector," Opt. Express **21**(25), 31548–31559 (2013).

21. H. Lu, X. Gan, B. Jia, D. Mao, and J. Zhao, "Tunable high-efficiency light absorption of monolayer graphene via Tamm plasmon polaritons," Opt. Lett. **41**(20), 4743–4746 (2016).

22. X. Wang, X. Jiang, Q. You, J. Guo, X. Dai, and Y. Xiang, "Tunable and multichannel terahertz perfect absorber due to Tamm surface plasmons with graphene," Photonics Res. **5**(6), 536–542 (2017).

23. S. Wang, G. Li, and Y. Zou, "Tunable Terahertz Absorption with Optical Tamm State in the Graphene-Bragg Reflector Configuration," Adv. Condens. Matter Phys. **2018**, 1–6 (2018).

24. Q. Zhang, X. Li, M. M. Hosain, Y. Xue, J. Zhang, J. Song, J. Liu, M. D. Turner, S. Fan, Q. Bao, and M. Gu, "Graphene surface plasmons at the near-infrared optical regime," Sci. Rep. **4**(1), 6559 (2015).

25. B Han, V. K. Tomer, T. A. Nguyen, A. Farmani, and P. K. Singh, *Nanosensors for Smart Cities*, Elsevier Publishing, 2020, ISBN 978-0-12-819870-4

26. M. Greiner, M. Helander, W.-M. Tang, Z.-B. Wang, J. Qiu, and Z.-H. Lu, "Universal energy-level alignment of molecules on metal oxides," Nat. Mater. **11**(1), 76–81 (2012).

27. C. Peng, R. Hamerly, M. Soltani, and D. Englund, "Design of high-speed phase-only spatial light modulators with two-dimensional tunable microcavity arrays," Opt. Express **27**(21), 30669 (2019).

28. Q. Bao and K. P. Loh, "Graphene Photonics, Plasmonics, and Broadband Optoelectronic Devices," ACS Nano **6**(5), 3677–3694 (2012).

29. Z. Chen, I. Santoso, R. Wang, L. F. Xie, H. Y. Mao, H. Huang, Y. Z. Wang, X. Y. Gao, Z. K. Chen, D. Ma, A. T. S. Wee, and W. Chen, "Surface transfer hole doping of epitaxial graphene using MoO3 thin film," Appl. Phys. Lett. **96**(21), 213104 (2010).

30. Z. Chen, X. Chen, L. Tao, K. Chen, M. Long, X. Liu, K. Yan, R. Stantchev, E. Pickwell-MacPherson, and J.-B. Xu, "Graphene controlled Brewster angle device for ultra broadband terahertz modulation," Nat. Commun. **9**(1), 4909 (2018).

31. G. Liang, X. Hu, X. Yu, Y. Shen, L. H. Li, A. G. Davies, E. Linfield, H. K. Liang, Y. Zhang, S. F. Yu, and Q. J. Wang, "Integrated Terahertz Graphene Modulator with 100% Modulation Depth," ACS Photonics **2**(11), 1559–1566 (2015).
32. V. Shautsova, T. Sidiropoulos, X. Xiao, N. Güsken, N. Black, A. Gilbertson, V. Giannini, S. Maier, L. Cohen, and R. Oulton, "Plasmon induced thermoelectric effect in graphene," Nat. Commun. **9**(1), 5190 (2018).